Performance and stability of the double absorbing boundary method for acoustic-wave propagation

Toby Potter[1], Jeffrey Shragge[2], and David Lumley[3]

ABSTRACT

The double absorbing boundary (DAB) is a novel extension to the family of high-order absorbing boundary condition operators. It uses auxiliary variables in a boundary layer to set up cancellation waves that suppress wavefield energy at the computational-domain boundary. In contrast to the perfectly matched layer (PML), the DAB makes no assumptions about the incoming wavefield and can be implemented with a boundary layer as thin as three computational grid-point cells. Our implementation incorporates the DAB into the boundary cell layer of high-order finite-difference (FD) techniques, thus avoiding the need to specify a padding region within the computational domain. We tested the DAB by propagating acoustic waves through homogeneous and heterogeneous 3D earth models. Measurements of the spectral response of energy reflected from the DAB indicate that it reflects approximately 10–15 dB less energy for heterogeneous models than a convolutional PML of the same computational memory complexity. The same measurements also indicate that a DAB boundary layer implemented with second-order FD operators couples well with higher-order FD operators in the computational domain. Long-term stability tests find that the DAB and CPML methods are stable for the acoustic-wave equation. The DAB has promise as a robust and memory-efficient absorbing boundary for 3D seismic imaging and inversion applications as well as other wave-equation applications in applied physics.

INTRODUCTION

The 3D acoustic-wave equation has numerous applications in many fields of applied physics. Of particular interest to computational geophysicists is the use of the acoustic-wave equation in advanced full-wavefield seismic imaging and inversion techniques such as reverse time migration (RTM) and full-waveform inversion (FWI). Applications of RTM include seismic exploration for hydrocarbon resources (Baysal et al., 1983; McMechan, 1983; Whitmore, 1983; Etgen et al., 2009), imaging the earth's lithosphere using earthquake wavefields (Shang et al., 2012), nondestructive testing (Anderson et al., 2011), and laser-ultrasound investigations (Johnson et al., 2015, 2017; Shragge et al., 2015). Examples of FWI applications include not only hydrocarbon exploration (Tarantola, 1984; Pratt et al., 1998; Virieux and Operto, 2009) but also ocean acoustic tomography (e.g., Munk et al., 2009), global tomography

of the earth's structure (Fichtner, 2010), and civil engineering (Wang et al., 2016).

The key computational kernel in 3D seismic imaging and inversion algorithms is two-way wave propagation through complex 3D media, often using the acoustic approximation. These algorithms use a wave-equation solver to propagate acoustic waves causally and acausally (i.e., forward and backward in time) through an estimated earth velocity model. A wide variety of numerical solution techniques exists for the two-way acoustic-wave equation, including finite-difference (FD) (e.g., Alford et al., 1974; Tam and Webb, 1993), finite-element (e.g., Marfurt, 1984; Bangerth and Rannacher, 1999), and spectral-element (e.g., Marfurt, 1984; Seriani and Priolo, 1994; Bangerth and Rannacher, 1999; Zampieri and Pavarino, 2006) methods. We restrict the discussion herein to finite-difference time-domain (FDTD) techniques; however, the absorbing boundary methods discussed herein are likely to be more broadly applicable.

[1]Formerly The University of Western Australia, Centre for Energy Geoscience, School of Earth Sciences, Crawley 6009, Australia; presently Pelagos Consulting and Education, Perth, Australia. E-mail: toby@pelagos-consulting.com.
[2]Formerly The University of Western Australia, Centre for Energy Geoscience, School of Earth Sciences, Crawley 6009, Australia; presently Colorado School of Mines, Center for Wave Phenomena, Geophysics Department, Golden, Colorado, USA. E-mail: jshragge@gmail.com (corresponding author).
[3]Formerly University of Texas at Dallas, School of Natural Sciences and Mathematics, Dallas, Texas, USA; presently University of Western Australia, School of Physics, Mathematics and Computing, Perth, Australia. E-mail: david.lumley@utdallas.edu.

Because computational efficiency of two-way FDTD computational kernels is dependent on the number of grid-point cells, efficiency can be significantly improved if the computational domain is only as large as the region of interest. The corresponding trade-off is that undesirable reflections from the computational-domain boundary can interfere with wavefield components throughout the model domain, leading to imaging and inversion artifacts.

A significant body of research has been devoted to developing absorbing-boundary operators that suppress wavefield energy impinging on the computational-domain boundary and prevent artificial reflections from propagating back into the domain interior. Givoli (2008) lists the key features of an ideal absorbing boundary: (1) The numerical problem must be mathematically well-posed such that a unique solution exists and the performance of the boundary operator yields a smoothly varying function of the input; (2) the discrete representation must be a sufficiently accurate approximation of the continuous physical system; (3) the numerical scheme of the absorbing boundary must be stable, compatible with that used for the interior, and efficient in the use of computing resources; (4) the boundary should perform well in a wide variety of problems, such as with heterogeneous absorbing and nonabsorbing media, different wave types, and varying orders of accuracy for the underlying numerical technique. Specifically for seismic imaging and inversion applications, the ability to time reverse the absorbing-boundary operator is very important to implement adjoint imaging and adjoint-state inversion methods (Fink et al., 2000; Plessix, 2006). An efficient boundary is also crucial for maintaining scalability in applications, especially for those using domain decomposition. Finally, in RTM and FWI applications, the long-term computational stability of the boundary condition is vital. We define "long-term stability" as a condition that the total wavefield energy within the computational domain remains constant or decreases over the duration needed for a wave to complete one or more complete crossings of the longest computational-domain axis.

Finding an absorbing boundary that fulfills all the above criteria remains an active topic of research. In recent years, two major classes of effective absorbing boundaries have emerged: artificial boundaries and artificial layers. In artificial-boundary schemes, a paraxial approximation is used in a boundary region to cancel reflections at the domain boundary. The family of artificial boundary techniques became known as an absorbing boundary condition (ABC) (Clayton and Engquist, 1977; Engquist and Majda, 1977; Reynolds, 1978; Bayliss and Turkel, 1980; Cerjan et al., 1985). Starting with Collino (1993), later formulations extended the ABC to higher-order accuracy through the use of auxiliary variables (Givoli, 2004; Hagstrom and Warburton, 2004).

Artificial-layer operators emerged in the mid-1990s as the second major class of absorbing boundary. The perfectly matched layer (PML), introduced by Berenger (1994), applies a complex coordinate stretch that results in the acoustic wavefield being exponentially attenuated because it propagates within the layer. The performance of the PML is directly related to the rate of wavefield attenuation, and a whole family of PML methods has arisen due to different implementations of the stretching function. We refer readers interested in implementation details to Teixeira and Chew (2000) and Bermúdez et al. (2007). More recent PML implementations, such as the convolutional PML (CPML), also use auxiliary variables to represent the modified wave equation in the absorbing layer (Kuzuoglu and Mittra, 1996; Roden and Gedney, 2000; Pasalic and McGarry, 2010). The

CPML has advantages over the PML in that it uses thinner boundary regions and more effectively dampens low-frequency wavefield components (Bécache et al., 2004).

ABCs and PMLs (including hybrid ABC schemes, Liu and Sen, 2010) have been shown to be equally effective at removing wavefield energy (Rabinovich et al., 2010), with each method having advantages and drawbacks. Classic ABCs can be implemented to any desired level of accuracy up to the discretization error; however, the complexity of handling high-order derivatives (e.g., $\mathcal{O}(\Delta x^4)$ and higher), especially at corners, provides a practical limitation between $\mathcal{O}(\Delta x^2)$ and $\mathcal{O}(\Delta x^3)$ (Bayliss and Turkel, 1980; Hagstrom et al., 2014). In contrast, PMLs are more straightforward to implement than ABCs, particularly at corners. PMLs, though, require significant parameter tuning due to the mapping from a continuous to a discrete problem (Baffet et al., 2014; Hagstrom et al., 2014; La-Grone and Hagstrom, 2016). In particular, these mapping issues are expressed by a lack of a rigorous convergence analysis and may lead to difficulties in specifying an optimal set of tuning parameters. The performance of the PML is essentially a function of the tuning parameters, discretization, PML layer width, and the wavefield itself.

The double absorbing boundary (DAB) method (Hagstrom et al., 2014) represents an evolution on existing ABC methods. It aims to have the same ease of implementation as the PML, while having the ability to converge on higher-order accuracy. Like the ABC, a DAB reduces the need for parameter tuning because it uses information from incoming waves to cancel artificial boundary reflections. Unlike the PML, the DAB makes no assumptions about incident wave type, which helps to forestall generation of numerical instabilities. Liu et al. (2015) tests the DAB in a 2D homogeneous velocity model and find that boundary reflection amplitudes compare favorably with a classic PML implementation (Berenger, 1994). They also use 2D synthetic data from a simulated 2D test of the SEG/EAGE Salt model (Aminzadeh et al., 1997) and find almost no artifacts attributable to the wavefield interaction with the DAB boundary.

In this paper, we test the DAB in a homogeneous model and the heterogeneous SEG/EAGE Salt model. We perform our model tests in 3D and modify the DAB to work with higher-order FDTD stencils and corners. Distinct from the work of Liu et al. (2015), we examine the spectral response of reflections from the DAB and compare the performance relative to the CPML in homogeneous and heterogeneous model domains and variable internal spatial discretizations. We also explore the long-term stability of the DAB, which is important for imaging and inversion algorithms such as RTM and FWI.

We begin by revisiting the theory of the acoustic-wave equation and the standard FDTD solution approach used herein. We then discuss the theory of the DAB method, describe our numerical implementation for 3D computational domains, and outline the extensions of the DAB to higher-order stencils. We discuss our spectral testing procedure and how it is applied to assess boundary performance in a test model. We then present our wave-propagation and spectral test results, including a direct comparison between the DAB and PML implementations for homogeneous and heterogeneous test models. Using the same models, we also explore the long-term stability of the DAB. The paper concludes with a discussion of various implementation issues that highlight the utility of the DAB as well as the need for undertaking additional future research.

THEORY

Wave propagation through a constant-density acoustic medium is governed by the acoustic-wave equation (Feynman et al., 1963):

$$\frac{1}{c^2}\frac{\partial^2 u}{\partial t^2} = \nabla^2 u + f, \tag{1}$$

where $u(\mathbf{x}, t)$ is the acoustic pressure wavefield defined over spatial and temporal variables $\mathbf{x}$ and t, respectively, $c(\mathbf{x})$ is the wave-propagation phase velocity, and $f(\mathbf{x}, t)$ is a source term. Although this equation formally represents the propagation of acoustic waves through an idealized fluid, it is commonly used in seismic imaging and inversion experiments as an approximation for P-wave propagation through isotropic elastic media.

Within a regularly sampled Cartesian grid, an $O(\Delta x^p)$ FD approximation to a partial derivative of order d at a point i is a dot product between D_m (a vector of M coefficients) and cells u_i^n along a dimension of the solution at time step n. The index i ranges from q cells before i, to r cells after i. If p is the desired order of accuracy, then $r = d + p - q - 1$, $M = d + p$, and

$$\frac{\partial^d u_i^n}{\partial x^d} = \frac{1}{\Delta x^d} \sum_{m=-q}^{d+p-q-1} D_m u_{i+m}^n + O(\Delta x^p). \tag{2}$$

We discretize the temporal derivatives in equation 1 using Taylor-series $O(\Delta t^2)$ central-difference coefficients with $q = 1$ and $r = 2$:

$$D_m = [1, -2, 1, 0]. \tag{3}$$

For the spatial derivatives, we use the $O(\Delta x^8)$ Taylor-series central-difference coefficients with $q = 4$:

$$D_m = \left[-\frac{1}{560}, \frac{8}{315}, -\frac{1}{5}, \frac{8}{5}, -\frac{205}{72}, \frac{8}{5}, -\frac{1}{5}, \frac{8}{315}, -\frac{1}{560}, 0\right]. \tag{4}$$

For centered FD approximations, we can safely omit the zero coefficient. We then use the discretized approximation to equation 1 to advance the 3D wavefield solution to the next time step $u_{i,j,k}^{n+1}$ according to

$$u_{i,j,k}^{n+1} = 2u_{i,j,k}^n - u_{i,j,k}^{n-1} + \Delta t^2 c_{i,j,k}^2 \left[\frac{1}{\Delta x^2} \sum_{m=-4}^{4} D_m u_{i+m,j,k}^n\right.$$

$$\left. + \frac{1}{\Delta y^2} \sum_{m=-4}^{4} D_m u_{i,j+m,k}^n + \frac{1}{\Delta z^2} \sum_{m=-4}^{4} D_m u_{i,j,k+m}^n\right], \tag{5}$$

where (i, j, k) are the 3D coordinate indices in the computational domain.

Double absorbing boundary

The DAB (Baffet et al., 2014; Hagstrom et al., 2014) behaves very much like noise-canceling headphones (Zangi, 1993). The difference is that ideally all of the incoming information (signal and noise) is removed, as opposed to removing only external noise. Figure 1 presents a schematic of the DAB implementation, simplified for just the right-hand boundary in one dimension. The DAB implements a high-order ABC in a boundary layer, Ω_B between the inner

(Γ_I) and the outer (Γ_E) surfaces. The interior of the computational domain Ω_M extends as far as the halo cells where the boundary between interior and halo cells is denoted by the extended vertical line. At Γ_I, the blue cells "sense" the incoming wavefield and use recursive one-way Hagstrom-Warburton (HW) (Hagstrom and Warburton, 2004) operators to construct cancellation waves that propagate across the DAB layer Ω_B. Figure 1 illustrates the wavefield and colocated cancellation waves propagating across Ω_B. At the orange cells of the outer boundary Γ_E, the propagated cancellation waves and the same recursive one-way HW operators are used to remove energy from $u(\mathbf{x}, t)$.

Cancellation waves propagated over the Ω_B boundary layer are organized in the form of a "ladder" of auxiliary variables $[\phi_0, \phi_1, \ldots, \phi_N]$. The auxiliary variables higher up the ladder may be thought of as correction terms to variables on lower rungs. The number of auxiliary variables depends on the desired order of accuracy $\mathcal{O}(\Delta x^N)$. The bottom rung of the ladder ϕ_0 is equivalent to the wavefield solution $u(\mathbf{x}, t)$. The auxiliary variables on each rung of the ladder are wavelike and propagate across the DAB layer using a low-order $\mathcal{O}(\Delta x^2, \Delta t^2)$ numerical approximation of equation 1. Hagstrom et al. (2014) describe a set of recursion operators that are used to traverse up and down the ladder at injection point Γ_I and external boundary Γ_E

$$a_j\frac{\partial\phi_j}{\partial t} + c\frac{\partial\phi_j}{\partial\eta} + \sigma_j\phi_j = a_{j+1}\frac{\partial\phi_{j+1}}{\partial t} - c\frac{\partial\phi_{j+1}}{\partial\eta} + \sigma_{j+1}\phi_{j+1}, \tag{6}$$

where η is oriented normal to the DAB layer and the DAB stencil constants σ_i and a_i are defined in the range $0 < a_j, a_{j+1} \le 1$ and $\sigma_j, \sigma_{j+1} \ge 0$ (Baffet et al., 2014).

Hagstrom and Warburton (2009) and Baffet et al. (2014) explore optimal choices for a_j, a_{j+1} and σ_j, σ_{j+1}. If T is the maximum simulation time and θ is an angle in the range $(0, \pi/2)$, Hagstrom and Warburton (2009) uses the following parameterization for a_j and σ_j:

$$a_j = \cos(\theta_j) \quad \text{and} \quad \sigma_j = \frac{\sin^2\theta_j}{T\cos\theta_j}. \tag{7}$$

For theoretical and implementation simplicity, we set $\theta_{j+1} = 0$ unless specified otherwise. This results in $a_j = 1$ and $\sigma_j = 0$, which may
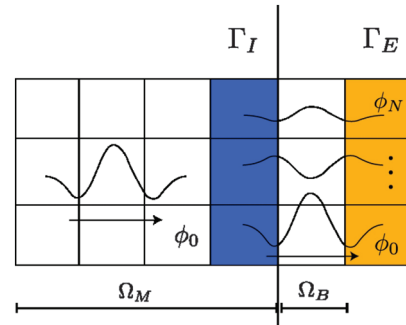

Figure 1. Schematic of a right-hand DAB region showing inner and outer boundaries Γ_I and Γ_E respectively. The interior of the computational modeling domain, Ω_M, includes cells at the injection layer Γ_I of the DAB. The DAB layer region Ω_B is located between Γ_I and Γ_E. The boundary between halo cells and interior cells is shown as an extended vertical line. The wavefield $u \equiv \phi_0$ is sampled at Γ_I, and cancellation waves $\phi_1 \ldots \phi_N$ are initiated in the DAB region as variables. The solution ϕ_0 is attenuated at the outer boundary Ω_B.

not be optimal in all cases, but nonetheless eliminates extra free parameters. Our computational tests show that it provides a very acceptable result and satisfies our goal of finding a general and robust DAB implementation that works well in the range of cases most likely to be encountered in exploration seismology.

Due to the minus sign on the right side in equation 6, cancellation waves on each rung on the auxiliary variable ladder are opposite in polarity to the one previous. Cancellation waves on the higher rungs of the ladder can be thought of as finer corrections to the wavefield on the rung immediately below it. At the outer boundary Γ_E and on the highest rung of the auxiliary variable ϕ_N, the system is closed by the boundary condition:

$$a_N \frac{\partial \phi_N}{\partial t} + c \frac{\partial \phi_N}{\partial \eta} + \sigma_N \phi_N = 0. \tag{8}$$

For initial conditions, we set $\phi_j = 0$, $\partial \phi_j / \partial t = 0$, and $\partial \phi_j / \partial \eta = 0$ because the wavefield is presumed quiescent in the boundary region at the first time step.

In practice, one first copies the updated solution at the next time step u^{n+1} to the lower rung of the ladder at the injection boundary Γ_I and then updates the auxiliary variables on each rung of the ladder to the next time step using equation 1. This provides an updated solution ϕ_{j+1}^{n+1} for all auxiliary variables in the DAB layer. One then uses equation 6 to ascend the ladder of wavefield corrections at the injection location Γ_I. This produces auxiliary variables ϕ_{j+1}^{n+1} at the injection boundary Γ_I for the next $n + 1$ time step. At all points in the outer boundary Γ_E, one enforces the boundary condition in equation 8 to produce the terminal variable ϕ_N^{n+1}. Finally, equation 6 is used at Γ_E to descend the ladder of wavefield corrections from ϕ_N^{n+1} back to ϕ_0^{n+1}, producing ϕ_j^{n+1}. Thus, we arrive at an updated value for ϕ_0^{n+1}, which is copied back to the solution u^{n+1} at all co-located points in the halo layer of the computational domain.

Numerical implementation

Following Hagstrom et al. (2014), we discretize the ladder operators and termination condition using an unconditionally stable implicit Crank-Nicolson scheme (Crank and Nicolson, 1947). We use a convention where index e (as in $\phi_{j,e}^n$) represents a boundary point and index i (as in $\phi_{j,i}^n$) indicates a point just inside the interface, but within the DAB layer. This convention applies to either the Ω_E or Ω_I interfaces.

Using this convention, we discretize equation 6 using second-order spatial and temporal central-difference approximations centered on the boundary between $\phi_{j,e}$ and $\phi_{j,i}$. Defining $\bar{c} = (c_i + c_e)/2$ as the average velocity across the interface and $\Delta \eta \equiv (e - i)\Delta x \equiv \pm \Delta x$, the discretized form of equation 6 is

$$\frac{a_j}{\Delta t}[\phi_{j,e}^{n+1} - \phi_{j,e}^n + \phi_{j,i}^{n+1} - \phi_{j,i}^n] + \frac{\bar{c}}{\Delta \eta}[\phi_{j,e}^{n+1} - \phi_{j,i}^{n+1} + \phi_{j,e}^n - \phi_{j,i}^n]$$

$$+ \frac{\sigma_j}{2}[\phi_{j,e}^{n+1} + \phi_{j,i}^{n+1} + \phi_{j,e}^n + \phi_{j,i}^n]$$

$$= \frac{a_{j+1}}{\Delta t}[\phi_{j+1,e}^{n+1} - \phi_{j+1,e}^n + \phi_{j+1,i}^{n+1} - \phi_{j+1,i}^n]$$

$$- \frac{\bar{c}}{\Delta \eta}[\phi_{j+1,e}^{n+1} - \phi_{j+1,i}^{n+1} + \phi_{j+1,e}^n - \phi_{j+1,i}^n]$$

$$+ \frac{\sigma_{j+1}}{2}[\phi_{j+1,e}^{n+1} + \phi_{j+1,i}^{n+1} + \phi_{j+1,e}^n + \phi_{j+1,i}^n]. \tag{9}$$

Sufficient care should be taken to ensure that the correct signs of $\Delta \eta$ and $\bar{c}$ are applied because the underlying equation is a directionally dependent one-way operator. Hence, $\bar{c}$ and η are signed because $e > i$ and $e < i$ are possible combinations. Regrouping terms,

$$\phi_{j,e}^{n+1}\left(a_j\Delta\eta + \bar{c}\Delta t + \frac{\sigma_j}{2}\Delta t\Delta\eta\right) + \phi_{j,e}^n\left(-a_j\Delta\eta + \bar{c}\Delta t + \frac{\sigma_j}{2}\Delta t\Delta\eta\right)$$

$$+ \phi_{j,i}^{n+1}\left(a_j\Delta\eta - \bar{c}\Delta t + \frac{\sigma_j}{2}\Delta t\Delta\eta\right)$$

$$+ \phi_{j,i}^n\left(-a_j\Delta\eta - \bar{c}\Delta t + \frac{\sigma_j}{2}\Delta t\Delta\eta\right)$$

$$= \phi_{j+1,e}^{n+1}\left(a_{j+1}\Delta\eta - \bar{c}\Delta t + \frac{\sigma_{j+1}}{2}\Delta t\Delta\eta\right)$$

$$+ \phi_{j+1,e}^n\left(-a_{j+1}\Delta\eta - \bar{c}\Delta t + \frac{\sigma_{j+1}}{2}\Delta t\Delta\eta\right)$$

$$+ \phi_{j+1,i}^{n+1}\left(a_{j+1}\Delta\eta + \bar{c}\Delta t + \frac{\sigma_{j+1}}{2}\Delta t\Delta\eta\right)$$

$$+ \phi_{j+1,i}^n\left(-a_{j+1}\Delta\eta + \bar{c}\Delta t + \frac{\sigma_{j+1}}{2}\Delta t\Delta\eta\right), \tag{10}$$

and defining constants

$$k_0 = \Delta\eta\left(a_j + \frac{\sigma_j}{2}\Delta t\right), \tag{11}$$

$$k_1 = \Delta\eta\left(-a_j + \frac{\sigma_j}{2}\Delta t\right), \tag{12}$$

$$k_2 = \Delta\eta\left(a_{j+1} + \frac{\sigma_{j+1}}{2}\Delta t\right), \tag{13}$$

$$k_3 = \Delta\eta\left(-a_{j+1} + \frac{\sigma_{j+1}}{2}\Delta t\right), \tag{14}$$

allows us to compactly rewrite equation 10 as

$$\phi_{j,e}^{n+1}(k_0 + \bar{c}\Delta t) + \phi_{j,e}^n(k_1 + \bar{c}\Delta t)$$

$$+ \phi_{j,i}^{n+1}(k_0 - \bar{c}\Delta t) + \phi_{j,i}^n(k_1 - \bar{c}\Delta t)$$

$$= \phi_{j+1,e}^{n+1}(k_2 - \bar{c}\Delta t) + \phi_{j+1,e}^n(k_3 - \bar{c}\Delta t)$$

$$+ \phi_{j+1,i}^{n+1}(k_2 + \bar{c}\Delta t) + \phi_{j+1,i}^n(k_3 + \bar{c}\Delta t). \tag{15}$$

To traverse up the ladder at the internal boundary Γ_I, we use equation 15 to set the higher-order auxiliary variables. Figure 2 depicts this process. We solve for the unknown vertex $\phi_{j+1,e}^{n+1}$ (shown in the yellow) in terms of the seven known (black) vertices, four from the previous time step n, two from $\phi_{j,i}^{n+1}$ and $\phi_{j+1,i}^{n+1}$, the updated points from the interior, and the newly derived point $\phi_{j,e}^{n+1}$ from a lower rung on the auxiliary variable ladder.

At the external boundary Γ_E, the following termination condition applies for $j = N$:

$$\phi_{N,e}^{n+1}(k_0 + \bar{c}\Delta t) + \phi_{N,e}^{n}(k_1 + \bar{c}\Delta t) + \phi_{N,i}^{n+1}(k_0 - \bar{c}\Delta t)$$
$$+ \phi_{N,i}^{n}(k_1 - \bar{c}\Delta t) = 0. \tag{16}$$

Figure 3 shows the graphical representation of equation 16. The unknown exterior point $\phi_{N,e}^{n+1}$, colocated with the external boundary Γ_E, is determined using ϕ_{e}^{n} from the previous time step as well as ϕ_{i}^{n} and ϕ_{i}^{n+1} from the solution to equation 1 in the interior DAB layer Ω_B.

To set the solution at the external boundary Γ_E, we apply equation 15 in reverse and descend the auxiliary variable ladder. Figure 4 illustrates how we solve for the unknown vertex $\phi_{j,e}^{n+1}$ (shown in the yellow) in terms of the seven known (black) vertices from the previous time step n, updated points from the interior $\phi_{j,i}^{n+1}, \phi_{j+1,i}^{n+1}$, and the newly derived point $\phi_{j+1,e}^{n+1}$ from a higher rung on the auxiliary variable ladder.

We note that the recursive ladder structure allows the DAB method to be implemented to any order of accuracy up to the discretization error; however, the computational and memory costs of applying the DAB increase linearly with the order of accuracy. Thus, we examine the suitability and efficiency of lower-order solutions.

Extending the DAB to corners and high-order stencils

High-order FD stencils may require an extended number of boundary cells around the computational domain Ω_M. In such cases, one must extend the interior width of the DAB between Γ_I and Γ_E so as to avoid spurious reflections that arise where the outer portions of the high-order FD stencil encounter zeroed boundary cells. For example, a centered $\mathcal{O}(\Delta x^8)$ FD stencil needs a boundary layer four cells wide. We extend the width of the DAB layer so that the interior DAB cells and the exterior layer Γ_E cover the entire boundary layer region, Γ_E of the DAB coincides with the outermost boundary cell. The resulting total width of the DAB layer is five cells. Combined with Γ_E, this makes up the required four cells for the higher-order stencil.

At corners, we adopt the methodology outlined by LaGrone and Hagstrom (2016), where 2D and 3D corners use doubly and triply indexed auxiliary variables, respectively. For an M-dimensional grid, the auxiliary variable ladders are represented by $2M$-dimensional grids. The first M dimensions are spatial, and the next M hyper dimensions implement rungs of the auxiliary variable ladder for DAB boundaries in the first M spatial dimensions. The length along each hyperdimension is $N + 1$ if the unit vector of the corresponding spatial dimension intersects a DAB boundary; otherwise, it is equal to unity. For example, Figure 5 shows a 2D computational domain of size $(nx, nz = nx)$ that incorporates a corner. The figure shows three distinct DAB regions denoted by the rectangles with dashed edges: two face regions to the left of the figure and one corner region to the right.

The auxiliary variables in the (upper, right, and corner) DAB regions are represented by 4D arrays. In the right DAB region, the 4D auxiliary variables have shape $(5, nz - 6, N + 1, 1)$, whereas in the upper DAB region and in the corner, the 4D auxiliary variables have shapes $(nx - 6, 5, 1, N + 1)$ and $(5, 5, N + 1, N + 1)$, respectively. Cells within the DAB regions are labeled by the functions that affect them. Some cells may have more than one function applied and hence may have more than one label (e.g., "ae"). For cells with label (a), the solution is copied to the bottom rung of the face DAB region. Cells with label (b) contain the interior of the face DAB region, in which all auxiliary variables are updated using a $\mathcal{O}(\Delta x^2, \Delta t^2)$ FD approximation to equation 1. The termination condition of equation 16 is
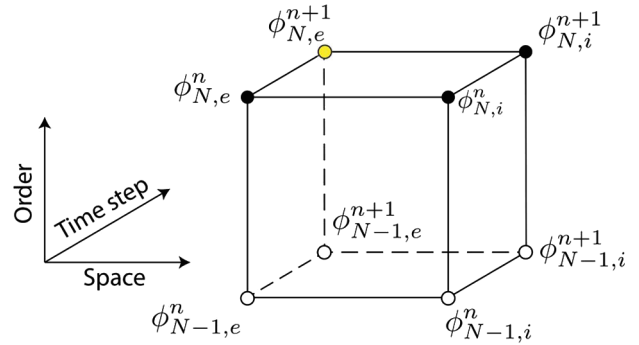

Figure 3. Applying the end closure boundary condition at the top of the auxiliary variable ladder where $j = N$. In this instance, the external boundary e corresponds to Γ_E. The unknown (yellow) vertex is obtained using the known vertices (black). The white vertices do not contribute to the solution.
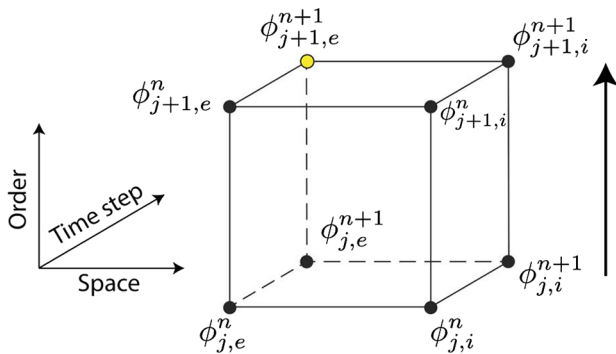

Figure 2. Traversing up the auxiliary variable ladder from j to $j + 1$, in this instance, the external boundary e corresponds to Γ_I. The unknown vertex (yellow) is solved for using the seven known vertices (black), four from the previous time step n, two from updated points from the interior $\phi_{j,i}^{n+1}$, and $\phi_{j+1,i}^{n+1}$, and the recently derived point $\phi_{j,e}^{n+1}$ from a lower rung on the auxiliary variable ladder.
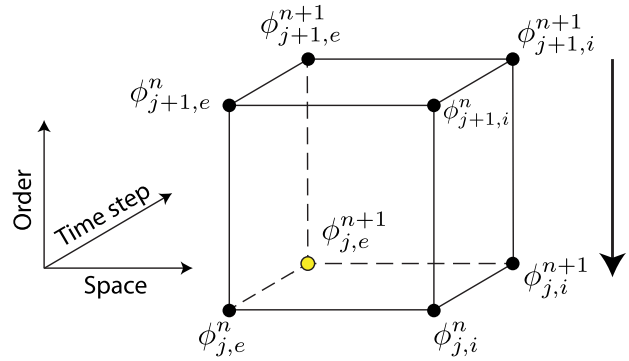

Figure 4. Traversing down the ladder from $j + 1$ to j, in this instance, the external boundary e is Γ_E. We solve for the unknown vertex $\phi_{j,e}^{n+1}$ (shown in the yellow) in terms of the known vertices (black) from the previous time step n, updated points from the interior $\phi_{j,i}^{n+1}, \phi_{j,i}^{n+1}$, and the newly derived point $\phi_{j+1,e}^{n+1}$ from a higher rung on the auxiliary variable ladder.

applied to cells with label (c), and the recursive relationship in equation 15 is applied to cells with labels (d) and (e) to descend and ascend the auxiliary variable ladders, respectively. In the corner DAB region, the auxiliary variables are copied from the face DAB regions to the corner DAB at cells with label (f). When copying arrays, care must be taken to include all transverse rungs of the DAB ladder from the face DAB regions. For example, when copying to the corner from the right DAB region, the subregion containing cells with label (f) to be copied, has shape $(3, 1, N + 1, 1)$, and when copying from the upper DAB region, the subregion to be copied to cells labeled (f) has shape $(1, 3, 1, N + 1)$. Then, all auxiliary variables are updated for cells with label (g) in the corner DAB using the $\mathcal{O}(\Delta x^2, \Delta t^2)$ FD approximation to equation 1. The termination conditions are subsequently applied for cells with label (h), and the recursive relations are again used for cells with labels (i) and (j) to descend and ascend the DAB ladder. Cells with label (k), including transverse hyperdimensions, are copied back to the face DAB regions, and, finally, cells with label (l) are copied back to the solution ready for the next update. For an in-depth description of the corner implementation, we refer readers to LaGrone and Hagstrom (2016).

Extending the DAB methodology to 3D implementations is relatively straightforward. A 3D domain has 6 faces, 8 corners, and 12 edge corners. At the edge corners, two of three hyperdimensions have extent $N + 1$, whereas the other has extent 1. The faces each have auxiliary variables with extent $N + 1$ only in the hyperdimension corresponding to a spatial dimension normal to the DAB. For each dimension that intersects a DAB boundary the same procedure is used: Memory is copied into Γ_E, the auxiliary variables are updated, termination conditions are applied, and the recursive relations are used to go up and down the layer at Γ_I and Γ_E. Copies to and from the DAB layer depend on the type of DAB boundary: Faces first copy from the main grid, edge corners then copy from faces, and, finally, corners copy from edge corners. Care must be taken to reverse the order when copying back, and all copies for rung zero on a particular hyperdimension must include all rungs from the other hyperdimensions.

Memory and computational complexity

The compute requirements for the DAB are minimal if a low-order method is used. If B is the number of points in the DAB boundary layer (not including injection cells), $d = 1$ is the number of injection cells, and N is the order of the method, then the total number of extra
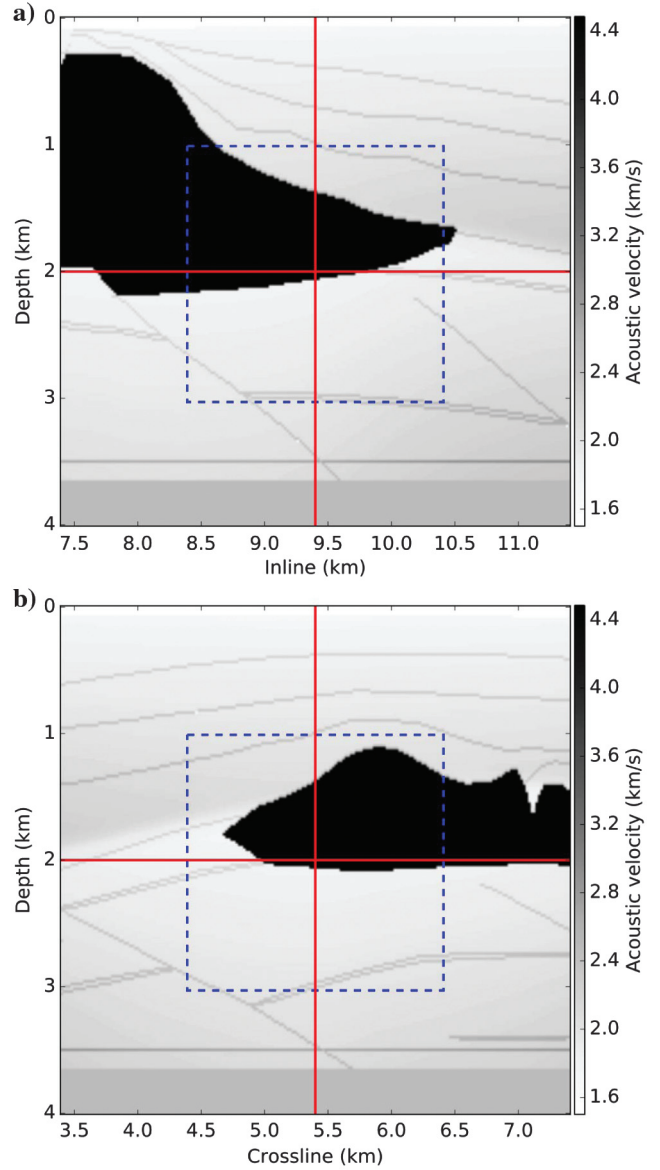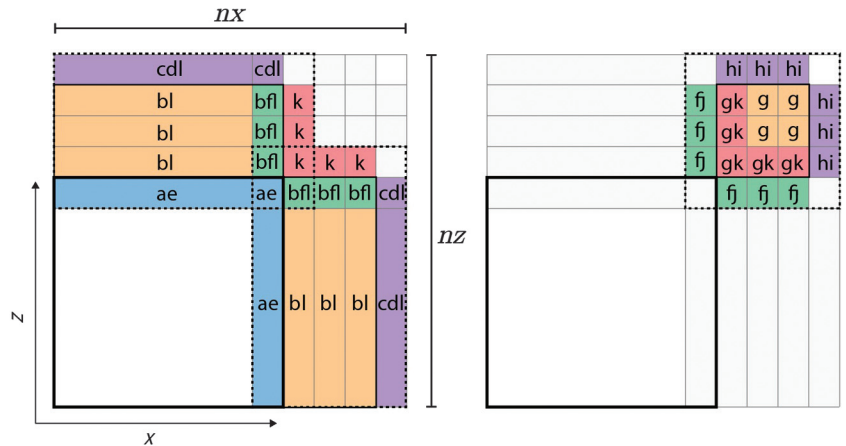

Figure 6. (a) Inline and (b) crossline section extracted from the reference model subsection of the 3D SEG/EAGE Salt model. The blue segmented box shows the area used for testing boundary conditions, and the red crosshair indicates the source location.

Figure 5. The DAB at a corner for a high-order stencil with a boundary layer four cells thick. The interior of the computational domain is denoted by the square with thick edges. Three DAB regions are shown: two face DAB regions on the left and one corner DAB region on the right. Information is copied to the DAB regions at cells with labels (a and f), auxiliary variables in the interior are updated at cells with labels (b and g), termination conditions are applied at cells with labels (c and h), the recursive relations in equation 15 are applied to traverse up the ladder at cells with labels (e and j), and down the ladder at cells with labels (d and i). Finally, information is copied back — first from the corner into the faces at cells with label (k) then from the faces into the solution at cells with label (l).

cells allocated per face boundary of area A is approximately $(B + d)(N + 1)A$. Similarly, a minimal centered FD implementation of the CPML (see Appendix A) requires storing a minimum of $2A(B + 1)$ extra cells per face. Therefore, if the lowest-order DAB method is implemented with $N = 1$, and $B = 4$, then an equivalent CPML boundary with identical memory requirements has a width B of four cells.

In terms of raw floating-point operations (FLOPS), the DAB is slightly more expensive than the CPML. For a 3D face boundary, propagating the cancellation waves across the DAB boundary requires a minimum of $10A(B - 1)(N + 1)$ fused multiply add FLOPS

for a second-order centered FD approximation. Applying the end condition and traversing up and down the auxiliary variable ladder requires about $A(4 + 16N)$ FLOPS if the constants in equations 15 and 16 are precomputed. Using $N = 1$, $d = 1$, and $B = 4$, $80A$ FLOPS are required per time step to update the DAB boundary per face. For 3D problems, the CPML method only needs two auxiliary variables per face of the computational domain (Kuzuoglu and Mittra, 1996; Roden and Gedney, 2000; Pasalic and McGarry, 2010). If a second-order centered FD method is used, the CPML method requires a minimum of $13A(B - 1)$ FLOPS for solving the modified wave equation (equation A-10) plus $8A(B - 1)$ FLOPS for updating the auxiliary variables (equation A-8), thus yielding $63A$ flops for the case where $B = 4$. If $B = 4$ and $A = 100$, then it is estimated that the CPML requires approximately 0.63 MegaFLOPS, which is close to the 0.80 MegaFLOPS needed to update the DAB. Latencies in moving data to and from memory reduce the importance of the different FLOPS counts shown here; therefore, memory usage comparisons have an arguably greater weight when comparing the DAB and CPML boundary operators.

TESTING PROCEDURE

In this section, we describe the procedure for several numerical tests designed to test the efficacy of our 3D DAB implementation in dampening reflections arising from the computational-domain boundary. The key metric we use in our tests is the *energy reflected* as a function of wavelength (in cells). We accomplish this by propagating a seismic wavelet from the center of a 201^3 reference model

Table 1. Propagation and model parameters for the homogeneous and heterogeneous velocity fields.

Model	Homogeneous	Heterogeneous
Grid size	101^3	101^3
Cell spacing (m)	20	20
Maximum velocity (m/s)	2716	4482
Minimum velocity (m/s)	2716	1500
Time step (ms)	2.21	1.34
T_{max} (s)	0.4	0.9
Peak frequency of source (Hz)	13.6	13.6
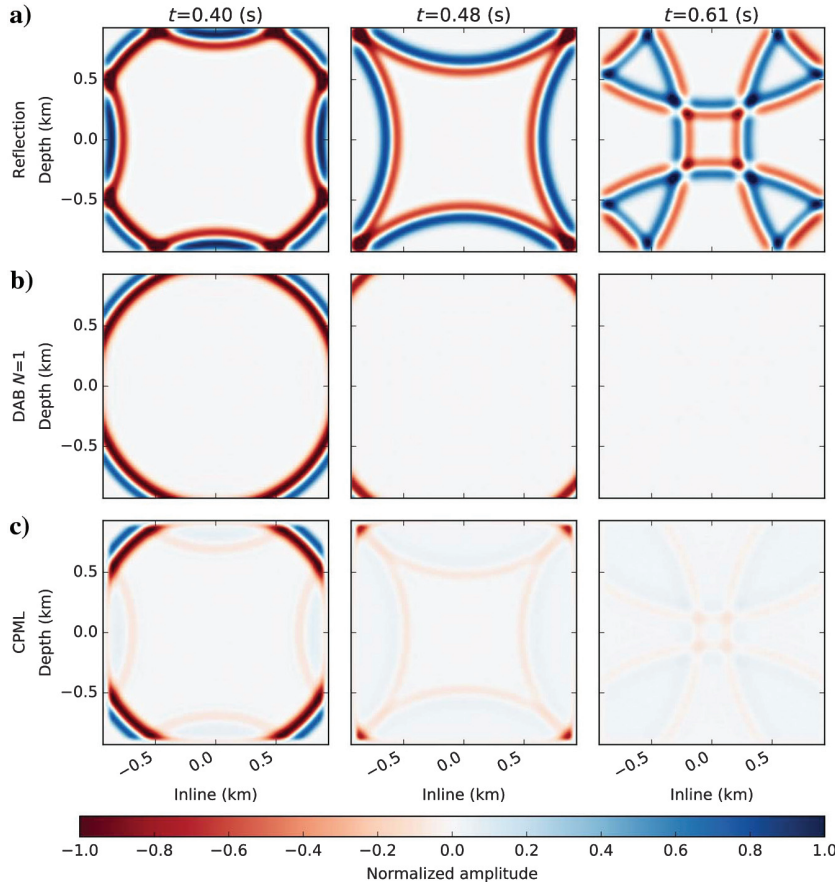
Figure 7. Application of different boundary conditions in the homogeneous test model. Each image is a cross section extracted halfway along the homogeneous test model, with the left, middle, and right columns showing the wavefield snapshots at $t = 0.40$, 0.48, and 0.61 s, respectively. The rows represent different boundary conditions: (a) reflecting; (b) DAB with $N = 1$ modified for $O(\Delta x^8)$ stencils; and (c) CPML with a layer width of four cells.

and halting the reference simulation prior to any wavefield component reaching the domain boundary. The reference wavefield is saved for comparison with that simulating in a smaller 101^3 "test" model, extracted from the center of the reference model.

After configuring the test model with the desired boundary, we again propagate the wavelet outward, but we compute a difference wavefield by subtracting the test wavefield from the corresponding volume of the reference wavefield. We obtain the spectrum of reflected energy per wavelength from the difference wavefield by applying a 3D Fourier transform to 3D wavefield snapshots, multiplying the result by its complex conjugate, and binning the result by Fourier wavenumber magnitude, $k = \sqrt{k_x^2 + k_y^2 + k_z^2}$. We use the average energy in each radial wavenumber bin as the *energy reflected*. We then average the energy reflected over all time steps after the initial wavefield interaction with the test domain boundary. Finally, we estimate boundary-layer attenuation values by dividing the time-averaged energy reflected spectrum by that obtained using the same procedure, but from a perfectly reflecting boundary in the test model. This approach is useful because it automatically accounts for energy from any reflections from heterogeneous structures embedded in the reference or test models.

We test the DAB performance by comparing wavefield simulations through homogeneous and heterogeneous P-wave velocity models. For the heterogeneous model, we use a subvolume of the SEG/EAGE 3D Salt model (Aminzadeh et al., 1997) with inline, crossline, and depth dimensions of $[x, y, z] = [13.52, 13.52, 4.2]$ km at a uniform $\Delta x = \Delta y = \Delta z = 20$ m cell discretization. We select a reference

model of size $nx \times ny \times nz = 201^3$ within this domain starting from the cell-centered position of $[x, y, z] = [7.4, 3.4, 0]$ km. The reference model encapsulates some salt-body features that represent challenging imaging and inversion targets. Nested within the reference model is the 101^3 test grid with an origin at [8.4, 4.4, 1.0] km. Figure 6 presents cross sections extracted from the reference model, with the test grid located within the overlain segmented blue box. We use the cell-centered position of [9.4, 5.4, 2.0] km for the shot location, marked by a red crosshair in Figure 6. For the homogeneous model, we use an identical computational domain as for the heterogeneous case, except for setting the acoustic P-wave velocity equal to the mean of the heterogeneous model ($V_P = 2716$ m/s).

Within the test models, we inject a 13.6 Hz central frequency Ricker wavelet (i.e., the second derivative of a Gaussian function) at the source position and propagate the wavefield using the 3D FDTD approach described above. At a frequency of 13.6 Hz and a mean velocity of $V_P = 2716$ m/s, the wavelength is approximately 160 m (eight cells) to reduce dispersion effects.

We adjust the propagation time step for each 3D model according to the multidimensional Courant-Frederichs-Levy (CFL) criteria (Courant et al., 1928):

$$C \equiv v_{\max} \Delta t \left[\frac{1}{\Delta x} + \frac{1}{\Delta y} + \frac{1}{\Delta z} \right] \leq 1, \qquad (17)$$

where $v_{\max}$ is the maximum velocity in the model. We use $C = 0.3$ in the 3D modeling test, which is within the CFL stability limit of

Figure 8. Application of different boundary conditions in the heterogeneous 3D SEG/EAGE Salt test model. Each image is a cross section taken halfway along the crossline axis. The left, middle, and right columns are wavefield snapshots extracted at times $t = 0.36$, 0.58, and 0.78 s, respectively. The rows represent different boundary conditions: (top) reflecting; (middle) DAB with $N = 1$ modified for $O(\Delta x^8)$ stencils; (bottom) CPML with a layer width of four cells.
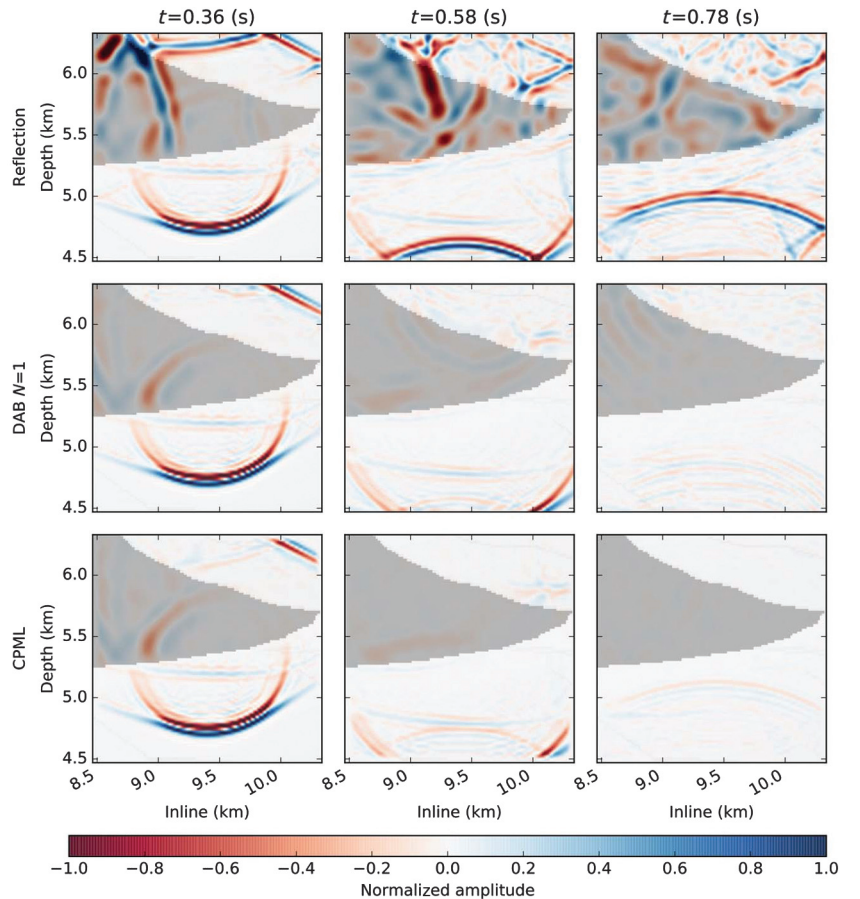
$C = 0.33$ for a 3D FDTD problem. For a spatial discretization of $\Delta x = \Delta y = \Delta z = 20$ m, this requires time-step intervals of $\Delta t = 1.34$ and $\Delta t = 2.21$ ms for the heterogeneous and homogeneous test models, respectively. We propagate the outwardly expanding wavefield through the test models until boundary reflections return to the center of the model. Table 1 presents the propagation parameters for the homogeneous and heterogeneous model tests.

At the edge of the test models, we apply the DAB boundary conditions for orders $N = 1, 4, 8, 12,$ and 16. We use one cell for the interior region of the DAB and keep the external boundary cells within the halo region. For comparison purposes, we also implement a CPML boundary operator (see Appendix A for details) using a CPML layer thickness of four cells in the internal domain located just inside the border of the boundary region. We use a CPML layer width of four cells because it has a memory requirement equivalent to that of the lowest-order DAB (i.e., $N = 1$), thereby allowing a direct comparison of the boundary operators in terms of reflected energy. For the homogeneous and heterogeneous model scenarios, we use an iterative grid search to tune the CPML parameters (here, $\sigma = 1768$ and $\alpha = 10.6$) to achieve optimal wavefield dampening.

RESULTS

Wavefield propagation

Figure 7 presents wavefield snapshots extracted from the 3D homogeneous model at times $t = 0.40, 0.48,$ and 0.610 s in the left,

center, and right columns, respectively. Within the homogeneous model, we observe that the DAB and CPML implementations (Figure 7b and 7c) do well at absorbing boundary reflections compared with a perfectly reflecting boundary (Figure 7a). The four-point CPML result exhibits weak boundary reflections caused by wavefield interactions with the leading edge of the PML region. We note this result could be improved by using a wider CPML region; however, this comes at additional computational cost and memory complexity.

Figure 8 presents 2D wavefield snapshots extracted from the 3D heterogeneous model at times $t = 0.36, 0.58,$ and 0.78 s. Figure 8 presents the wavefields, whereas Figure 9 shows the wavefields after subtracting the reference solution. The DAB and CPML implementations handle the heterogeneous salt/rock transitions in the top boundary; however, the CPML snapshots exhibit minor reflections from the top and bottom boundaries at $t = 0.36$ and 0.58 s, respectively. The DAB bounded wavefield snapshot at $t = 0.78$ s has wavefield energy in the top left corner of the boundary, which is not present in the CPML bounded model.

Spectral tests

Figure 10 presents the results of the spectral testing procedure described above. This plot presents the relative reflected energy (in dB) as a function of wavelength in terms of cells. Figure 10a and 10b presents the testing results for the homogeneous (heterogeneous) model. At short wavelengths (less than eight cells), the performance of both boundaries is significantly degraded relative to longer
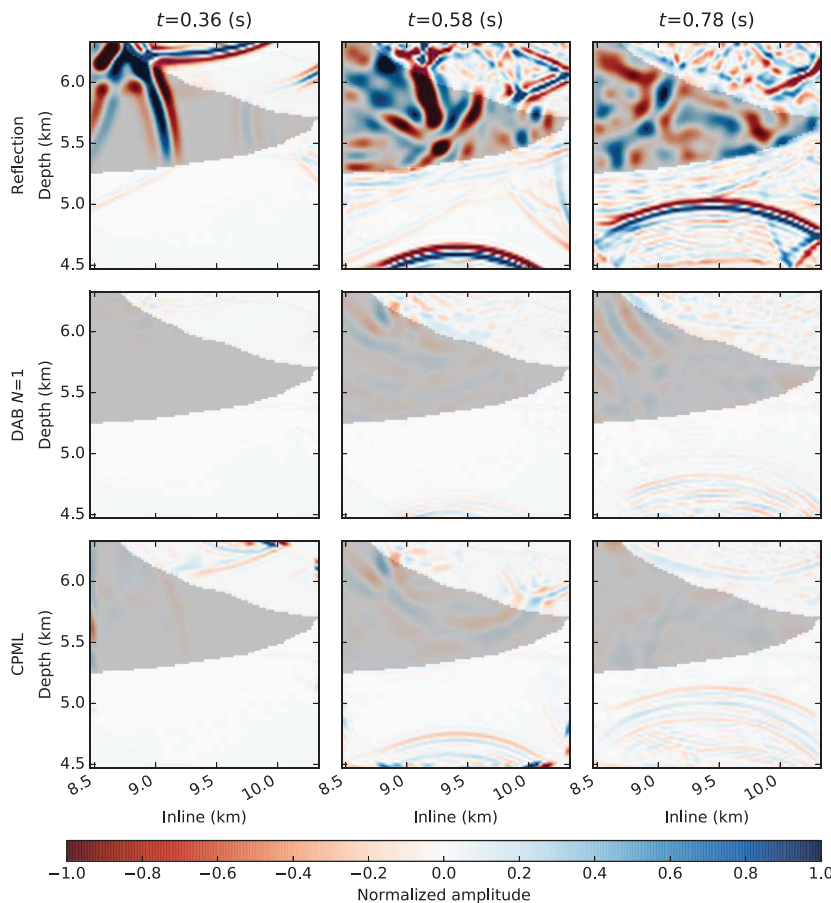

Figure 9. The same sequence of frames as in Figure 8; however, the wavefield in each frame has the reference solution subtracted. Each image is a cross section taken halfway along the crossline axis. The left, middle, and right columns are wavefield snapshots extracted at times $t = 0.36, 0.58,$ and 0.78 s, respectively. The rows represent different boundary conditions: (top) reflecting, (middle) DAB with $N = 1$ modified for $O(\Delta x^8)$ stencils, and (bottom) CPML with a layer width of four cells.

wavelengths. This is most likely due to numerical dispersion in which waves at short wavelengths are effectively propagated at erroneous velocities. For the homogeneous model, the DAB and CPML have similar performance, with an optimal reduction of energy, 25–27 dB, at wavelengths approximately 10–15 cells. The heterogeneous test model has a velocity structure more likely to be encountered in real-world applications. In that model, the DAB method reaches an energy reduction of 30 dB, which outperforms the CPML by approximately 10–15 dB. As shown in Figure 10, increasing the order of the DAB method from $N = 1$ to $N = 16$ (and thereby incurring an increase in computational cost) appears to make a negligible difference to the relative reflected energy.

The above tests have used an eighth-order spatial discretization operator in equation 5 to approximate a solution to equation 1 for the computational domain Ω_M, but they have used a second-order FD method to update the auxiliary variables in the DAB region. The coupling between high- and low-order methods at the boundary may reduce the accuracy of the DAB methods. We test this hypothesis using the aforementioned heterogeneous spectral test and changing the order of spatial discretization to second, fourth, and eighth order, respectively. Figure 11 shows the results, in which the time-averaged power spectra at second- and fourth-order discretizations are compared with the time-averaged power spectra at eighth-order discretization. For lower-order discretizations, the results show up to a 5 dB difference in absorbed power at wavelengths approaching Nyquist (i.e., between two and eight wavelengths). This indicates that a mismatch in discretization between the interior domain and DAB

region (e.g., $O(\Delta x^8)$ versus $O(\Delta x^2)$, respectively) does play a role; however, the differences are only apparent at dispersion-affected wavelengths shorter than the equivalent of eight cells. Outside the
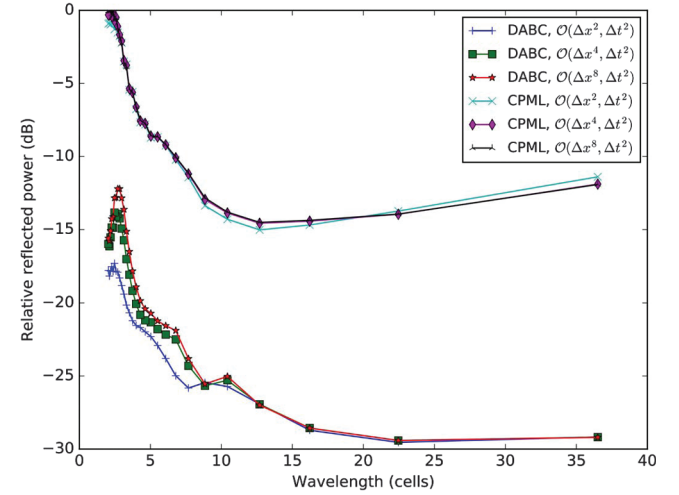

Figure 11. Power spectrum of wavefields in the heterogeneous model. The time-averaged relative power spectra of the lowest order DAB method with $N = 1$ and the CPML are shown. The order of spatial discretization in the Laplacian operator of equation 1 in the interior domain has been varied from $\mathcal{O}(x^2)$ to $\mathcal{O}(\Delta x^8)$, while keeping the $\mathcal{O}(\Delta x^2)$ discretization of the DAB boundary region.

Figure 10. Relative reflected energy as a function of wavelength (in cells) for the DAB and CPML implementations in (a) homogeneous and (b) heterogeneous test models. We plot the relative (to a pure reflection) reflected energy from the DAB method with increasing order of accuracy $N = 1 - 16$ and along with that obtained from the implemented CPML boundary.
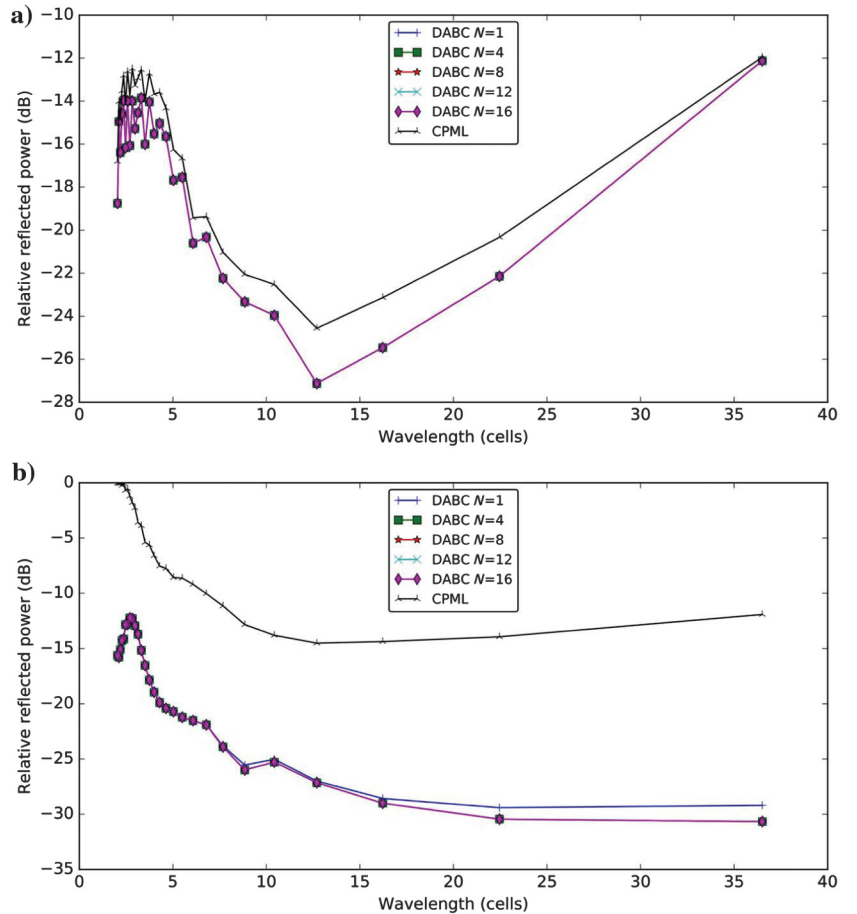
dispersive regime, the differences are negligible and all orders of discretization yield a similar response.

Long-term stability

We test the long-term stability of the DAB and CPML methods by running the test simulation up to a 10.0 s maximum simulation time for homogeneous and heterogeneous models. This corresponds to approximately 10 corner-to-corner wavefront crossing times for either models. We save the wavefield every three time steps and compute the energy within the grid at each saved time step. If N_c is the number of cells in the test model then we compute the average grid energy E at time step t as

$$E(t) = \frac{1}{N_c} \sum_i \sum_j \sum_k u_{i,j,k,t}^2(t). \qquad (18)$$

Figure 12a and 12b shows the time-varying grid energy relative to the energy from a simulation with purely reflective boundaries for the homogeneous and heterogeneous models, respectively. We examine several values for θ in equation 7, ranging from 0 to $4\pi/10$ and resulting in a corresponding range of values for of a_j and σ_j. Both models show negligible difference among the choices for θ. In both models, the DAB implementations achieve reductions approaching 40 dB, whereas the CPML achieves long-term reductions in energy exceeding 75 dB.

DISCUSSION

The DAB and CPML operators shown in Figures 7 and 8 appear to significantly reduce the wavefield energy. Due to the handling of DAB corners, we see little evidence of corner reflections at amplitudes greater than those from the faces. This suggests the corner boundary implementation of LaGrone and Hagstrom (2016) and Baffet et al. (2014) is sufficient for general use in heterogeneous media.

The spectral tests discussed above show that for a homogeneous velocity model and short time frames (i.e., less than two grid crossings), the untuned DAB and tuned CPML models of the same memory usage compare favorably in terms of energy reduction with a maximum attenuation of approximately 25–27 dB. The CPML performance is similar to that of the DAB because the homogeneous model is unlikely to propagate waves that break the plane-wave assumption on which the CPML depends. The same spectral test applied to a heterogeneous model velocity shows that the DAB achieves a reduction of approximately 30 dB, whereas the CPML reaches 15 dB. We attribute this performance improvement to the DAB being implemented with no assumptions on the nature of the incoming wavefield. In contrast, the family of PML methods is designed to dampen wavefields comprised of linear combinations of plane waves. Heterogeneous velocity models generate short-wavelength behavior that may break the plane-wave assumption; hence, the CPML performs suboptimally. For both models, at wavelengths of fewer than eight cells, the DAB or CPML showed suboptimal performance. This is most likely due to numerical dispersion effects.

As seen in Figure 11, lowering the order of the spatial discretization in the interior has a negligible effect at all but the most dispersion-affected wavelengths approximately — two to eight cells. Given the benefits of using high-order discretization in the interior domain, we suggest that the coupling of a higher-order method in the computational domain combined with a thin DAB boundary region with low-order discretization provides an acceptable means of absorbing energy while keeping computational costs and memory requirements low. In all tests of DAB methods, we saw negligible variation among the DAB parameters, when either the order (N) or angle (θ) was varied. This suggest that a simple DAB implementation with $N = 1$ will suffice for most DAB applications.

Simulations of wavefield propagation over several grid crossing times suggest that with corners implemented, the DAB and CPML methods are stable for long-term acoustic-wave propagation. DAB methods appear to asymptote to a 40 dB reduction in energy,
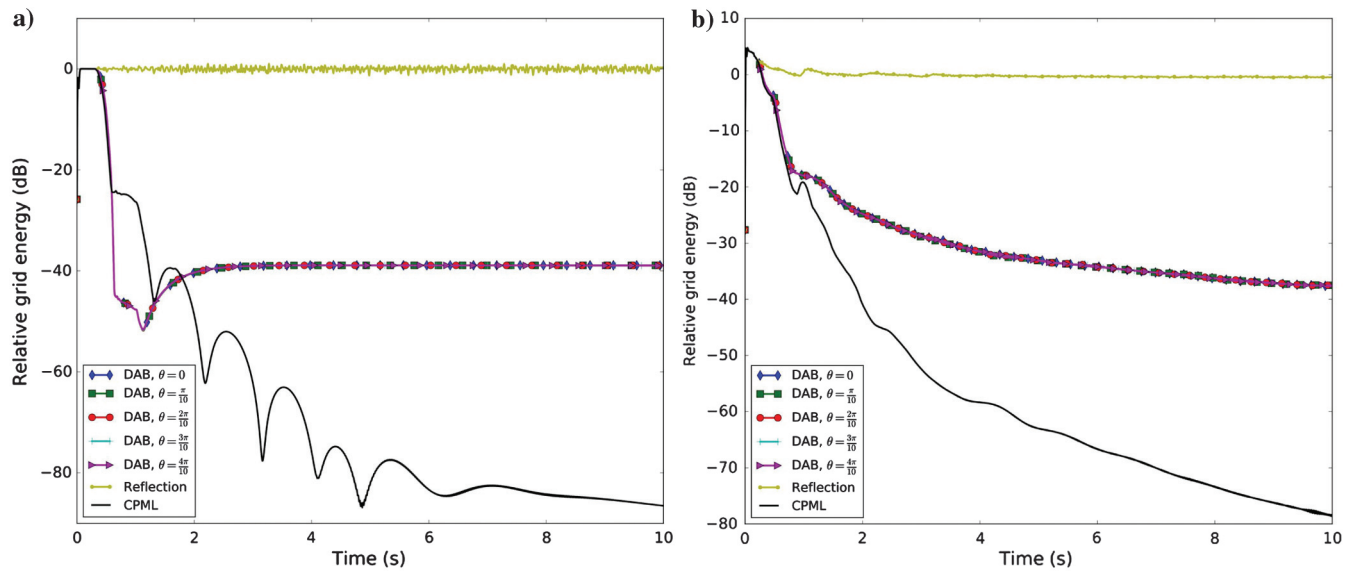

Figure 12. Relative grid energy for $t = 0 - 10$ s for the (a) homogeneous and (b) heterogeneous tests for the DAB and CPML implementations.

whereas the CPML appears to attenuate to more than 75 dB. For extended simulation times, the CPML achieves a much better long-term absorption of wavefield energy as a result of its multiplicative as opposed to the subtractive nature of the DAB.

Finally, although this study investigated the use of the DAB in isotropic acoustic wavefield simulation, we point out that previously published research examines the use of DABs in FDTD solvers for heterogeneous isotropic (Rabinovich et al., 2015) and certain classes of anisotropic (Rabinovich et al., 2017) 3D elastic media. Our additional as-yet-unpublished work has demonstrated that DABs can be applied to 3D equations of viscoelastodynamics, as well as in numerical solution strategies involving nonstaggered, singly staggered (i.e., time and space), and fully staggered grids (Lebedev, 1964; Lisitsa and Vishnevsky, 2010; Shragge and Tapley, 2017). However, further comparative work needs to be conducted to determine the (de)merits of using a DAB approach, relative to a CPML, for 3D viscoelastic wave-propagation scenarios in realistic 3D heterogeneous models.

CONCLUSION

This paper examines a DAB approach that combines the most beneficial aspects of traditional ABC and PML boundary methods. The DAB is fairly straightforward to implement and is effective even with very thin boundary regions, low-order discretizations, and single-precision floating-point arithmetic. We implement the DAB by embedding it in a boundary-layer region, thus avoiding the need to include a padding layer in the computational domain.

We extend the DAB method to high-order 3D FDTD applications, including corners, and we test the implementation by propagating a 13.6 Hz Ricker wavelet source through homogeneous and heterogeneous models and compare the DAB's reflected response to that produced by a CPML implementation of equivalent memory complexity. Our tests indicate that the effectiveness of the DAB and CPML approaches is reduced by numerical dispersion introduced at wavelengths shorter than eight cells. For a homogeneous model, the DAB and CPML perform similarly; however, for a heterogeneous velocity model, the DAB outperforms the CPML. We attribute the improved performance of the DAB over the CPML in heterogeneous environments on the former making no assumptions about the nature of the incoming waves, whereas the latter is theoretically designed to attenuate plane waves.

We find the DAB is effective even with the minimum number of rungs (i.e., $N = 1$) and second-order discretization for FD modeling in the DAB layer. When coupled with high-order interior discretization, the DAB remains effective for wavelengths larger than eight cells. Increasing the order of the DAB layer or adjusting the DAB stencil constants (a_j and σ_j) led to negligible improvements on the models reported herein; thus, they may be simplified to $a_j = 1$ and $\sigma_j = 0$. Long-term stability tests show that the CPML is superior at removing energy from the grid, which is probably due to its multiplicative (as opposed to subtractive) nature. Overall, we find that the DAB provides a better value for computing resources, when compared to a CPML boundary, for realistic heterogeneous 3D earth models.

Given the aforementioned results, we conclude that a low-order DAB method is well-suited to applications of 3D acoustic wavefield propagation through heterogeneous velocity models, such as those encountered in RTM and FWI analyses. The small number of required layer cells and the lack of parameter tuning makes the DAB method particularly attractive for use in full-wavefield acoustic imaging and inversion analyses for a variety of geophysical and other wave-physics-based applications.

DATA AND MATERIALS AVAILABILITY

Data associated with this research are available and can be obtained by contacting the corresponding author.

APPENDIX A

THE CONVOLUTIONAL PML

To provide an effective performance comparison of the DAB with other techniques, we implement a complex-frequency-shifted CPML (Kuzuoglu and Mittra, 1996; Roden and Gedney, 2000; Pasalic and McGarry, 2010). With the CPML technique, one achieves exponential wavefield dampening by applying a frequency-domain stretch of spatial coordinates $\mathbf{x}$ using the transformation:

$$d\tilde{x} = dx\left(1 + \frac{\sigma(x)}{\alpha + j\omega}\right), \qquad \text{(A-1)}$$

$$\tilde{x} = x + \frac{1}{\alpha + j\omega}\int^{x} \sigma(x')dx', \qquad \text{(A-2)}$$

where $j = \sqrt{-1}$. In these stretched coordinates, plane waves with solution $u(x, t) = \exp j(k_0 x - \omega_0 t)$ become

$$u(x, t) = \exp\, j(k_0 x - \omega_0 t)\exp\left(\frac{-k_0}{\omega_0 - aj}\int^{x}\sigma(x')dx'\right) \qquad \text{(A-3)}$$

and the solution is attenuated exponentially in the absorbing layer. Pasalic and McGarry (2010) suggests that the stretching function $S_i(x, \omega) = 1 + ((\sigma_i(x))/(\alpha_i + j\omega))$ in equation A-1 forms a modified derivative operator in the ith dimension of the transformed stretched coordinate space,

$$\frac{\partial}{\partial\tilde{x}} = \frac{1}{S_i(x)}\frac{\partial}{\partial x}. \qquad \text{(A-4)}$$

The equivalent time-domain operation is a temporal convolution operation,

$$\frac{\partial}{\partial \tilde{\eta}_i} = \mathcal{F}^{-1}\left(\frac{1}{S_i(x, \omega)}\right) * \frac{\partial}{\partial x_i}. \quad \text{(A-5)}$$

Implementing the convolution is made more efficient through the introduction of auxiliary variables ψ_i and ζ_i (Roden and Gedney, 2000) such that

$$\frac{\partial u}{\partial \tilde{x}_i} = \frac{\partial u}{\partial x_i} + \psi_i \quad \text{(A-6)}$$

and

$$\frac{\partial^2 u}{\partial \tilde{x}_i^2} = \left[\frac{\partial^2 u}{\partial x_i^2} + \frac{\partial \psi_i}{\partial x_i}\right] + \zeta_i. \quad \text{(A-7)}$$

Updates to the auxiliary variables are given by

$$\psi_i^{n+1} = a_i \psi_i^n + b_i \frac{\partial u^n}{\partial x_i} \quad \text{(A-8)}$$

and

$$\zeta_i^{n+1} = a_i \zeta^n + b_i \frac{\partial \psi_i^n}{\partial x_i}, \quad \text{(A-9)}$$

where the constants are given by $a_i = \exp(-(\sigma_i + \alpha_i)\Delta t)$ and $b_i = ((\sigma_i)/(\sigma_i + \alpha_i))(a_i - 1)$. In the PML region, the modified wave equation with N dimensions is then

$$\frac{\partial^2 u}{\partial t^2} - c^2\left[\nabla^2 u + \sum_{i=0}^{N-1}\frac{\partial \psi_i}{\partial x_i} + \sum_{i=0}^{N-1}\zeta_i\right] = 0. \quad \text{(A-10)}$$

REFERENCES

Alford, R., K. Kelly, and D. M. Boore, 1974, Accuracy of finite-difference modeling of the acoustic wave equation: Geophysics, **39**, 834–842, doi: 10.1190/1.1440470.

Aminzadeh, F., J. Brac, and T. Kunz, 1997, 3D salt and overthrust models: SEG.

Anderson, B., M. Griffa, P.-Y. L. Bas, T. J. Ulrich, and P. A. Johnson, 2011, Experimental implementation of reverse time migration for nondestructive evaluation applications: Journal of the Acoustical Society of America Express Letters, **129**, EL8–EL14, doi: 10.1121/1.3526379.

Baffet, D., T. Hagstrom, and D. Givoli, 2014, Double absorbing boundary formulations for acoustics and elastodynamics: SIAM Journal on Scientific Computing, **36**, A1277–A1312, doi: 10.1137/130928728.

Bangerth, W., and R. Rannacher, 1999, Finite element approximation of the acoustic wave equation: Error control and mesh adaptation: East West Journal of Numerical Mathematics, **7**, 263–282.

Bayliss, A., and E. Turkel, 1980, Radiation boundary conditions for wave-like equations: Communications on Pure and Applied Mathematics, **33**, 707–725, doi: 10.1002/cpa.3160330603.

Baysal, E., D. Kosloff, and J. Sherwood, 1983, Reverse-time migration: Geophysics, **48**, 1514–1524, doi: 10.1190/1.1441434.

Bécache, E., P. Petropoulos, and S. Gedney, 2004, On the long-time behavior of unsplit perfectly matched layers: IEEE Transactions on Antennas and Propagation, **52**, 1335–1342, doi: 10.1109/TAP.2004.827253.

Berenger, J.-P., 1994, A perfectly matched layer for the absorption of electromagnetic waves: Journal of Computational Physics, **114**, 185–200, doi: 10.1006/jcph.1994.1159.

Bermúdez, A., L. Hervella-Nieto, A. Prieto, and R. Rodrı, 2007, An optimal perfectly matched layer with unbounded absorbing function for time-harmonic acoustic scattering problems: Journal of Computational Physics, **223**, 469–488, doi: 10.1016/j.jcp.2006.09.018.

Cerjan, C., D. Kosloff, R. Kosloff, and M. Reshef, 1985, A nonreflecting boundary condition for discrete acoustic and elastic wave equations: Geophysics, **50**, 705–708, doi: 10.1190/1.1441945.

Clayton, R., and B. Engquist, 1977, Absorbing boundary conditions for acoustic and elastic wave equations: Bulletin of the Seismological Society of America, **67**, 1529–1540.

Collino, F., 1993, High order absorbing boundary conditions for wave propagation models. Straight line boundary and corner cases: 2nd International Conference on Mathematical and Numerical Aspects of Wave Propagation (Newark, DE, 1993), 161–171.

Courant, R., K. Friedrichs, and H. Lewy, 1928, Über die partiellen differenzengleichungen der mathematischen physik: Mathematische Annalen, **100**, 32–74.

Crank, J., and P. Nicolson, 1947, A practical method for numerical evaluation of solutions of partial differential equations of the heat-conduction type: Mathematical Proceedings of the Cambridge Philosophical Society, **43**, 50–67.

Engquist, B., and A. Majda, 1977, Absorbing boundary conditions for numerical simulation of waves: Proceedings of the National Academy of Sciences, **74**, 1765–1766.

Etgen, J., S. Gray, and Y. Zhang, 2009, An overview of depth imaging in exploration geophysics: Geophysics, **74**, no. 6, WCA5–WCA17, doi: 10.1190/1.3223188.

Feynman, R., R. Leighton, and M. Sands, 1963, The Feynman lectures on physics, 2nd ed.: Addison-Wesley.

Fichtner, A., 2010, Full seismic waveform modelling and inversion: Springer Science and Business Media.

Fink, M., D. Cassereau, A. Derode, C. Prada, P. Roux, M. Tanter, J.-L. Thomas, and F. Wu, 2000, Time-reversed acoustics: Reports on Progress in Physics, **63**, 1933–1995, doi: 10.1088/0034-4885/63/12/202.

Givoli, D., 2004, High-order local non-reflecting boundary conditions: A review: Wave Motion, **39**, 319–326, doi: 10.1016/j.wavemoti.2003.12.004.

Givoli, D., 2008, Computational absorbing boundaries, *in* Steffen, M., and N. Bodo, eds., Computational acoustics of noise propagation in fluids — Finite and boundary element methods: Springer-Verlag, 145–166.

Hagstrom, T., D. Givoli, D. Rabinovich, and J. Bielak, 2014, The double absorbing boundary method: Journal of Computational Physics, **259**, 220–241, doi: 10.1016/j.jcp.2013.11.025.

Hagstrom, T., and T. Warburton, 2004, A new auxiliary variable formulation of high-order local radiation boundary conditions: Corner compatibility conditions and extensions to first-order systems: Wave Motion, **39**, 327–338, doi: 10.1016/j.wavemoti.2003.12.007.

Hagstrom, T., and T. Warburton, 2009, Complete radiation boundary conditions: Minimizing the long time error growth of local methods: SIAM Journal on Numerical Analysis, **47**, 3678–3704, doi: 10.1137/090745477.

Johnson, J. L., J. Shragge, and K. van Wijk, 2015, Image reconstruction of multi-channel photoacoustic and laser-ultrasound data using reverse time migration: Proceedings of the SPIE 9323, Photons Plus Ultrasound: Imaging and Sensing.

Johnson, J. L., J. Shragge, and K. van Wijk, 2017, Nonconfocal all-optical laser-ultrasound and photoacoustic imaging system for angle-dependent deep tissue imaging: Journal of Biomedical Optics, **22**, 041014–041014, doi: 10.1117/1.JBO.22.4.041014.

Kuzuoglu, M., and R. Mittra, 1996, Frequency dependence of the constitutive parameters of causal perfectly matched anisotropic absorbers: IEEE Microwave and Guided Wave Letters, **6**, 447–449, doi: 10.1109/75.544545.

LaGrone, J., and T. Hagstrom, 2016, Double absorbing boundaries for finite-difference time-domain electromagnetics: Journal of Computational Physics, **326**, 650–665, doi: 10.1016/j.jcp.2016.09.014.

Lebedev, V., 1964, Difference analogues of orthogonal decompositions, basic differential operators and some boundary value problems: USSR Computational Mathematics and Mathematical Physics, **5**, 449–465.

Lisitsa, V., and D. Vishnevsky, 2010, Lebedev scheme for the numerical simulation of wave propagation in 3D anisotropic elasticity: Geophysical Prospecting, **58**, 619–635, doi: 10.1111/j.1365-2478.2009.00862.x.

Liu, Y., X.-Y. Li, and S.-Q. Chen, 2015, Application of the double absorbing boundary condition in seismic modeling: Applied Geophysics, **12**, 111–119, doi: 10.1007/s11770-014-0463-z.

Liu, Y., and M. Sen, 2010, A hybrid scheme for absorbing edge reflections in numerical modeling of wave propagation: Geophysics, **75**, no. 2, A1–A6, doi: 10.1190/1.3295447.

Marfurt, K. J., 1984, Accuracy of finite-difference and finite-element modeling of the scalar and elastic wave equations: Geophysics, **49**, 533–549, doi: 10.1190/1.1441689.

McMechan, G. A., 1983, Migration by extrapolation of time-dependent boundary values: Geophysical Prospecting, **31**, 413–420, doi: 10.1111/j.1365-2478.1983.tb01060.x.

Munk, W., P. Worcester, and C. Wunsch, 2009, Ocean acoustic tomography: Cambridge University Press.

Pasalic, D., and R. McGarry, 2010, Convolutional perfectly matched layer for isotropic and anisotropic acoustic wave equations: 80th Annual International Meeting, SEG, Expanded Abstracts, doi: 10.1190/1.3513453.

Plessix, R.-E., 2006, A review of the adjoint-state method for computing the gradient of a functional with geophysical applications: Geophysical Journal International, **167**, 495–503, doi: 10.1111/gji.2006.167.issue-2.

Pratt, R., C. Shin, and G. Hicks, 1998, Gauss-Newton and full Newton methods in frequency-space seismic waveform inversions: Geophysical Journal International, **133**, 341–362.

Rabinovich, D., D. Givoli, and E. Becache, 2010, Comparison of high-order absorbing boundary conditions and perfectly matched layers in the frequency domain: International Journal of Numerical Methods in Biomedical Engineering, **26**, 1351–1369, doi: 10.1002/cnm.1394.

Rabinovich, D., D. Givoli, J. Bielak, and T. Hagstrom, 2015, The double absorbing boundary method for elastodynamics in homogeneous and layered media: Advanced Modeling and Simulation in Engineering Sciences, **2**, 1–27.

Rabinovich, D., D. Givoli, J. Bielak, and T. Hagstrom, 2017, The double absorbing boundary method for a class of anisotropic elastic media: Computer Methods in Applied Mechanics and Engineering, **315**, 190–221, doi: 10.1016/j.cma.2016.10.035.

Reynolds, A. C., 1978, Boundary conditions for the numerical solution of wave propagation problems: Geophysics, **43**, 1099–1110, doi: 10.1190/1.1440881.

Roden, J. A., and S. D. Gedney, 2000, Convolutional PML (CPML): An efficient FDTD implementation of the CFS-PML for arbitrary media: Microwave and Optical Technology Letters, **27**, 334–339, doi: 10.1002/1098-2760(20001205)27:5<334::AID-MOP14>3.0.CO;2-A.

Seriani, G., and E. Priolo, 1994, Spectral element method for acoustic wave simulation in heterogeneous media: Finite Elements in Analysis and Design, **16**, 337–348, doi: 10.1016/0168-874X(94)90076-0.

Shang, X., M. V. de Hoop, and R. D. van der Hilst, 2012, Beyond receiver functions: Passive source reverse time migration and inverse scattering of converted waves: Geophysical Research Letters, **39**, L15308, doi: 10.1029/2012GL052289.

Shragge, J., T. E. Blum, K. Van Wijk, and L. Adam, 2015, Full-wavefield modeling and reverse time migration of laser ultrasound data: A feasibility study: Geophysics, **80**, no. 6, D553–D563, doi: 10.1190/geo2015-0020.1.

Shragge, J., and B. Tapley, 2017, Solving the tensorial 3D acoustic wave equation: A mimetic finite-difference time-domain approach: Geophysics, **82**, no. 4, T183–T196, doi: 10.1190/geo2016-0691.1.

Tam, C. K., and J. C. Webb, 1993, Dispersion-relation-preserving finite difference schemes for computational acoustics: Journal of Computational Physics, **107**, 262–281, doi: 10.1006/jcph.1993.1142.

Tarantola, A., 1984, Inversion of seismic reflection data in the acoustic approximation: Geophysics, **49**, 1259–1266, doi: 10.1190/1.1441754.

Teixeira, F. L., and W. C. Chew, 2000, Complex space approach to perfectly matched layers: A review and some new developments: International Journal of Numerical Modelling: Electronic Networks, Devices and Fields, **13**, 441–455, doi: 10.1002/1099-1204(200009/10)13:5<441::AID-JNM376>3.0.CO;2-J.

Virieux, J., and S. Operto, 2009, An overview of full-waveform inversion in exploration geophysics: Geophysics, **74**, no. 6, WCC1–WCC26, doi: 10.1190/1.3238367.

Wang, H., A. Che, S. Feng, and X. Ge, 2016, Full waveform inversion applied in defect investigation for ballastless undertrack structure of high-speed railway: Tunnelling and Underground Space Technology, **51**, 202–211, doi: 10.1016/j.tust.2015.10.035.

Whitmore, N., 1983, Iterative depth migration by backward time propagation: 53rd Annual International Meeting, SEG, Expanded Abstracts, 382–384, doi: 10.1190/1.1893867.

Zampieri, E., and L. F. Pavarino, 2006, Approximation of acoustic waves by explicit Newmark's schemes and spectral element methods: Journal of Computational and Applied Mathematics, **185**, 308–325, doi: 10.1016/j.cam.2005.03.013.

Zangi, K. C., 1993, A new two-sensor active noise cancellation algorithm: Proceedings of the IEEE International Conference on Acoustics, Speech, and Signal Processing, 351–354.